J Nanopart Res (2017) 19: 267
DOI 10.1007/s11051-017-3953-0

RESEARCH PAPER

Effect of the size of silver nanoparticles on SERS signal enhancement

Rui Xiu He · Robert Liang · Peng Peng · Y. Norman Zhou

Received: 10 February 2017 / Accepted: 5 July 2017 / Published online: 27 July 2017

Abstract The localized surface plasmon resonance arising from plasmonic materials is beneficial in solution-based and thin-film sensing applications, which increase the sensitivity of the analyte being tested. Silver nanoparticles from 35 to 65 nm in diameter were synthesized using a low-temperature method and deposited in a monolayer on a (3-aminopropyl)triethoxysilane (APTES)-functionalized glass slide. The effect of particle size on monolayer structure, optical behavior, and surface-enhanced Raman scattering (SERS) is studied. While increasing particle size decreases particle coverage, it also changes the localized surface plasmon resonance and thus the SERS activity of individual nanoparticles. Using a laser excitation wavelength of 633 nm, the stronger localized surface plasmon resonance coupling to this excitation wavelength at larger particle sizes trumps the loss in surface coverage, and greater SERS signals are observed. The SERS signal enhancement accounts for the higher SERS signal, which was verified using a finite element model of a silver nanoparticle dimer with various nanoparticle sizes and separation distances.

Keywords Surface-enhanced Raman spectroscopy · Surface plasmon resonance · Silver nanoparticles · Size dependence · Sensors · Plasmonics · Instrumentation

R. X. He · R. Liang · P. Peng · Y. Norman Zhou
Department of Mechanical and Mechatronics Engineering, University of Waterloo, 200 University Avenue West, Waterloo, Ontario N2L 3G1, Canada

R. X. He · R. Liang · Y. Norman Zhou
Waterloo Institute for Nanotechnology, University of Waterloo, 200 University Avenue West, Waterloo, Ontario N2L 3G1, Canada

P. Peng
School of Mechanical Engineering and Automation, Beihang University, 37 Xueyuan Rd, Beijing 100191, China

P. Peng (✉)
International Research Institute for Multidisciplinary Science, Beihang University, 37 Xueyuan Rd, Beijing 100191, China
e-mail: ppeng@buaa.edu.cn

Introduction

Silver nanoparticles (Ag NPs) have been the focus of extensive research within the past two decades and have a wide range of practical applications (Chimentão et al. 2004; Aroca 2006; Ricco 2006; Le Ru et al. 2009; Alarifi et al. 2011; Dong et al. 2015; Rao et al. 2015; Shahid-ul-Islam et al. 2016). Metal NPs in general exhibit the localized surface plasmon resonance (LSPR) phenomenon at visible wavelengths, which refers to the driven oscillation of conduction electrons around the bulk of the NP by electromagnetic radiation. For this property, Ag NPs are primarily used in biochemical sensing as a detection label (Wang et al. 2003; Schrand et al. 2008), in metal-enhanced fluorescence (Aslan et al. 2005), or in surface-enhanced Raman spectroscopy (SERS) (Stiles et al. 2008; Oćwieja et al. 2015). Other plasmonic applications include Ag NP decoration to improve the visible light performance of UV

photocatalytic TiO_2 (Yu et al. 2009) or to act as light-trapping centers in thin-film solar cells (Tan et al. 2012).

A large body of work describes the application of Ag NPs immobilized on solid substrates, primarily as a low-cost and scalable approach to SERS substrates capable of producing nanostructures much smaller than lithographically possible (Bright et al. 1998; Goulet et al. 2005; Fan and Brolo 2009; Zhu et al. 2013; Lin et al. 2015; Wang et al. 2015). Gold NP-based SERS substrates are already commercially available, but due to their higher reactivity (Bright et al. 1998) and storage complications arising from oxidation (Han et al. 2011), Ag substrates are mainly synthesized in the lab as needed. A fundamental understanding of the Ag NP monolayer formation kinetics is starting to take form as the popularity of these substrates in research grows. Recently, Oćwieja et al. (2015) published a review consolidating much of the experimental literature on monolayer formation kinetics and proposed a hybrid theoretical model to describe monolayer formation and characteristics based on bulk solution properties like NP concentration, pH, ionic strength, NP size, and temperature. In general, in colloidal self-assembly, these properties govern the electrostatic interactions between the substrate and suspended and deposited NPs which ultimately determines final coverage and structure. These findings are useful for engineering Ag NP monolayers, particularly for tuning LSPR properties or optimizing SERS for different analytes and excitation sources as LSPR activity is directly related to the SERS enhancement factor (EF) (Haynes and Van 2003).

In this work, spherical Ag NPs were synthesized and deposited in a monolayer on a (3-aminopropyl)triethoxysilane (APTES)-functionalized glass slide, and the structure, LSPR, and SERS performance were evaluated. The behavior of the LSPR has been studied extensively (Kelly et al. 2003; Behnajady et al. 2009; Cobley et al. 2009; Qin et al. 2010) and experimentally (Cobley et al. 2009; Qin et al. 2010; Bastús et al. 2014). However, a discussion of the effect of particle size and its effect on SERS continues to be of interest (Tian et al. 2013). The largest SERS enhancement sites are situated in the nanoscale gaps between NP dimers, and analytes adsorbed in these "hot spots" are thought to be responsible for the majority of the SERS signal (Etchegoin et al. 2006). Increasing particle size decreases the final particle coverage (Oćwieja et al. 2015), which diminishes the number of hot spots situated in the SERS excitation area and thus decreases the signal. However, it has been demonstrated that EF is greatest when LSPR is correctly correlated with the chosen excitation wavelength (Haynes and Van 2003). This experiment studies the effect of increasing the particle size on the monolayer number density and SERS signal. Finite element modeling is used to study the particle size effect on plasmon strength and to explain the experimental results.

Experimental

Materials

Silver nitrate ($AgNO_3$) (Premion™ 99.9995%), trisodium citrate (TSC) (>99%), and ascorbic acid (AA, >99%) were obtained from Alfa Aesar. Polyvinylpyrrolidone (PVP) (Mw = 55K), (3-aminopropyl)triethoxysilane (APTES) (>99%), and rhodamine 6G (R6G) (>99%) were obtained from Sigma-Aldrich. Ammonium hydroxide (ACS), hydrogen peroxide (30%), sulfuric acid (ACS), and glass slides were obtained from Fisher. Ultra-pure water obtained from a Durpro filtration system ($\rho > 18.2$ MΩ) was used throughout the experiments.

Synthesis of silver nanoparticle solutions

Ag NPs from 34.9 to 64.6 nm in diameter were synthesized by a two-step reaction starting with the synthesis of Ag seeds, followed by seed growth by ascorbic acid reduction of $AgNO_3$. Seeds were synthesized by preparing a 100-mL solution of 0.3 mM TSC and 0.25 mM $AgNO_3$ in an ice bath. The solution was left to cool with stirring for over 10 min; then, 3 mL 10 mM $NaBH_4$ was added dropwise every 5 s. The solution was stirred for an additional 30 min in the ice bath then stored in a household refrigerator at 4 °C for up to 1 month prior to use. The resultant solution consisted of 4-nm-diameter seeds at a concentration of 1.1×10^{-7} M. Ag NPs of different sizes were synthesized by preparing a 100-mL solution containing Ag seeds, TSC, PVP, and 46 μmol $[Ag(NH_3)_2]^+$ under stirring. A solution of 0.1 M AA was then added dropwise, waiting for the solution to complete any color changes prior to adding the next drop (about 30 s) until no more color changes were observed. Five solutions were used in this study, herein referred to as $NP_{1 \rightarrow 5}$. Amounts of reagents were calculated based on keeping the PVP and TSC content per available Ag surface area constant and are summarized in Table 1.

Table 1 Synthesized silver nanoparticles of various sizes

Identifier	Seed (mL)	PVP (μmol)	TSC (μmol)	Measured diameter[a] (nm)
NP_1	1.69	14.8	133	34.9
NP_2	0.21	7.36	65.9	39.5
NP_3	0.06	4.90	43.9	47.2
NP_4	0.03	3.68	32.9	56.4
NP_5	0.01	2.94	26.3	64.6

[a] Size characterization based on NPs immobilized on substrate

Fabrication of silver nanoparticle monolayer substrates

Glass slides were cleaned in boiling piranha etch ($1H_2O_2$:$4H_2SO_4$ stock solution by volume) diluted to 10% in water at 90 °C for 1 h. A solution of 1%vol. APTES was prepared during this time and allowed to hydrolyze for >15 min. The slides were removed from the piranha, rinsed with water, and immersed in the APTES solution upright for 1 h to functionalize the surface. The substrates were then rinsed with water and dried in a convection oven at 80 °C for 2 h. Ag NP monolayers were formed by NP immobilization on the functionalized slides by immersion in Ag NP solution upright for 48 h. The substrates were then removed, rinsed with water, and then drawn out of the water bath by a dip coater at 1 mm/min lifting speed to ensure even drying. The silver monolayer immobilization process is depicted in Fig. 1. The substrates were used immediately after drying for the study to avoid oxidative effects from atmospheric exposure (Han et al. 2011).

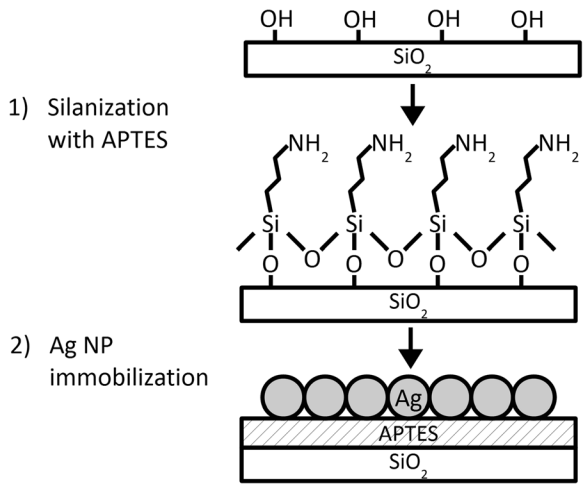

Fig. 1 Schematic of self-assembly strategy for the fabrication of Ag NP monolayer substrates. First, the glass surface is functionalized with a silence molecule providing a high density of positively-charged NH_2 groups. Then, the negatively charged Ag NPs are immobilized by electrostatic attraction

Instrumentation

Raman spectra were acquired by a Renishaw Raman Dual System 1000. The Raman excitation source was a HeNe laser with a wavelength of 632.8 nm focused on the sample through a ×50 objective lens. Laser power was measured to be 4.53 mW, and acquisition time was always 10 s per individual spectrum. UV/vis absorption spectra were acquired by a Shimadzu UV-2501PC. Scanning electron microscopy was performed on a ZEISS LEO 1550 FE-SEM.

Results and discussion

Particle size effect on substrate microstructure

SEM imaging was used to characterize the distribution of the silver nanoparticles on the substrate (Fig. 2). The particles immobilized on glass substrate are quasi-spherical and found either alone or in clusters in a monolayer. As the particle size increases, the solutions become more polydisperse, with the standard deviation in size increasing from 7% for NP_1 up to 23% for NP_4. While the amounts of TSC and PVP added were scaled with final surface coverage, they affect the initial solution conditions during the nucleation and early growth stages, which are the same for all batches. Thus, the ratio of surfactant to seed surface area is much higher for the NP_5 batch, compared to the NP_1 since the amount of seed was reduced while the amount of surfactant was increased. This dramatically altered the solution ionic strength during the initial stages of growth and resulted in a polydisperse solution. Nonetheless, we were still able to achieve increasing average particle sizes which could be used to elucidate the size-dependent properties of SERS.

A common barrier for self-assembly-based metal NP SERS substrates for achieving quantitative detection is spot-spot signal reproducibility (Stiles et al. 2008). Since the beam diameter used for SERS excitation is about 1 μm, short-range variance in the substrate coverage is smoothed across this relatively large area. Generally, final particle coverage decreases as the diameter increases. One study showed that solution concentration mainly affected the initial uptake rate of Ag NPs on a polyelectrolyte surface, while maximum coverage depended on solution ionic

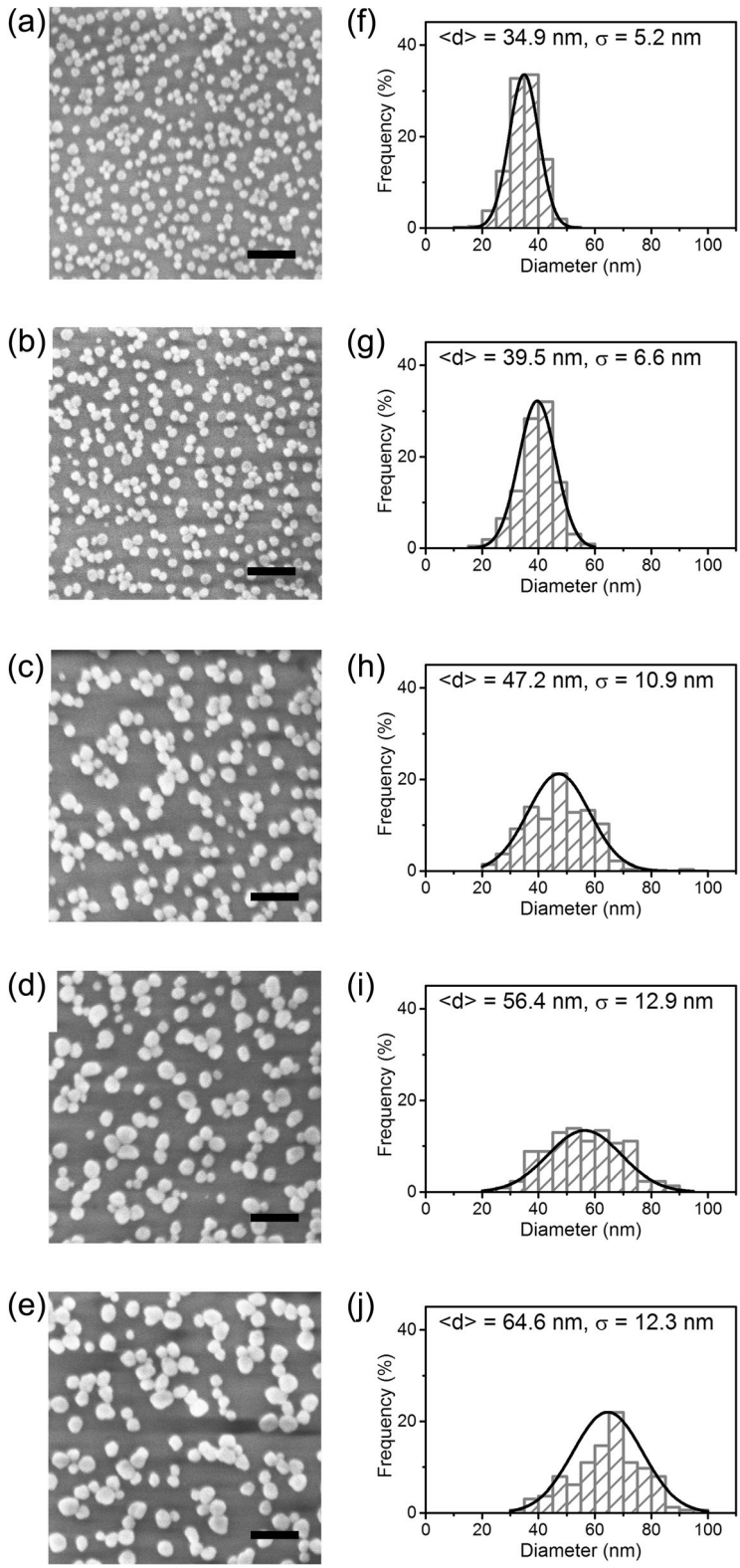

Fig. 2 **a**–**e** SEM micrographs of substrates from NP_1 to NP_5, respectively. **f**–**j** Particle size distribution on substrates $NP_1 \rightarrow NP_5$, respectively, with a Gaussian fit. <*d*> denotes average diameter, and σ is the standard deviation. The *scale bar* (*black*) is set at 200 nm

strength by addition of NaCl (Oćwieja et al. 2012). Another study looked at the effect of monovalent and divalent chloride salt electrolytes on the aggregation kinetics and found that attachment efficiency increases with ionic strength (Huynh and Chen 2011). These agree with the finding that while initial uptake is based on electrostatic attraction between the positively charged substrate and the negatively charged NPs, particle agglomeration induced by particle-particle collisions (Grabar et al. 1996) determines the final NP coverage. The result is a substrate characterized by lone and clustered NPs in a uniform surface density at the micron scale.

In this study, PVP is included as a surfactant. PVP has been shown to shield Ag NPs from chloride, sulfate, and nitrate environmental changes where trisodium citrate and polyethylene glycol failed (Tejamaya et al. 2012). It more strongly adsorbs onto the Ag surface than TSC, and steric repulsion of the polymer chains prevents agglomeration in solution (Huynh and Chen 2011). By using APTES as a polyelectrolyte supporting layer with 48 h deposition time, maximum coverage is attained on all substrates. However, ionic strength of the solution was not controlled for. TSC concentration ranged from 26 μM to 1.3 mM for NP_5 to NP_1, which is relatively low and does not significantly affect attachment efficiency (Huynh and Chen 2011). Combined with the charge screening effect of PVP, for which the amount was scaled with the total NP surface area, the interaction range of all the NP solutions remains roughly constant. Under this assumption, the interaction range, h, can be obtained by fitting to the random sequential adsorption (RSA) model for particles interacting via a screened Coulomb potential, which predicts the maximum particle coverage for NP monolayers (Oćwieja et al. 2015). For spherical particles, maximum coverage θ_M can be approximated by Oćwieja et al. (2015).

$$\theta_M = \frac{\theta_0}{\left(1+\frac{2h}{d}\right)^2}$$

where θ_0 is the maximum coverage for non-interacting particles (0.547 for spheres), and d is the particle diameter. The predicted surface density at saturation is given as

$$N_s = \frac{4\theta_0}{\pi\left(d^2+2h\right)}.$$

Figure 3 plots the surface density vs. diameter and shows a fit of θ_M in the RSA model. Using a least-squares fitting algorithm, h is predicted to be 17.2 nm,

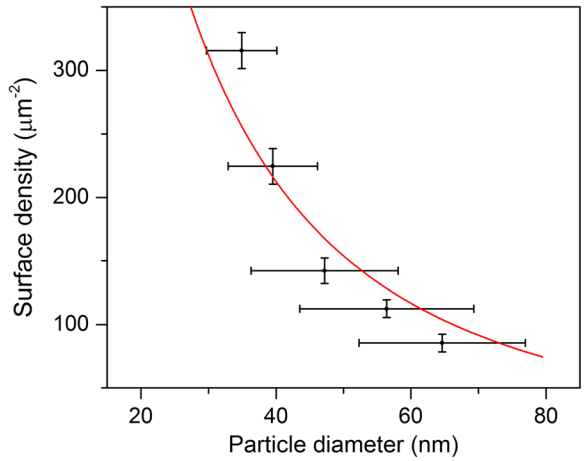

Fig. 3 Dependence of the NP surface density on diameter. *Error bars* indicate standard deviation. The surface density refers to the average number of NPs from three SEM images of dimensions 1.2 μm × 0.8 μm. The red curve was generated by a fit to the RSA model for NP adsorption on polyelectrolyte substrates

with $R^2 = 0.86$. This value is slightly lower than reported for hydrodynamic diameters for various Ag NPs in solution (El Badawy et al. 2010; Oćwieja et al. 2013; Morga et al. 2014), which can be explained by the fact that NPs immobilize in clusters. In fact, since particle agglomeration is the main mechanism of particle immobilization near saturation, the RSA model is insufficient to describe the final coverage as complex interactions involving surfactants and agents in the liquid medium may take place. In this case, there is a deviation from the RSA model, where NPs immobilize in higher densities below 40 nm and lower densities above 40 nm.

Particle size effect on optical properties

UV/vis absorption spectroscopy was used to characterize the optical properties of both the NP solutions and substrates, shown in Fig. 4. This method reveals the LSPR profile of the substrates and can be used to estimate particle size with peak position and monodispersity with peak width (Haiss et al. 2007). The solutions show a primary LSPR peak characteristic of individual NP absorption from 400 to 440 nm. The peak heights steadily decrease, consistent with the decreasing concentration of NPs. By keeping the number of Ag^+ ions constant while decreasing the number of seeds, larger particles were obtained at lower concentration. A redshift and broadening occur with increasing particle size, in accordance with the increase in size and polydispersity. An exception to the redshift trend occurs

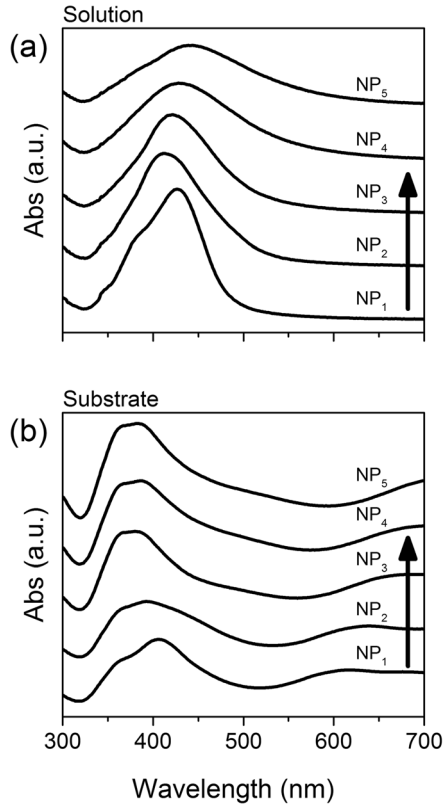

Fig. 4 UV/vis absorbance spectra of **a** NP solutions diluted 1:20 and **b** NP substrates. The direction of the arrow indicates an increase in size

with NP_1, which is thought to be explained by plasmon coupling to surrounding NPs due to the higher concentration of NPs (Zhao et al. 2003). A blueshift of the primary peak occurs from solution to substrate, attributed to the refractive index of water, which blueshifts the light apparent to the particles in solution (Paul J. G. Goulet et al. 2005). The substrates show an increase in absorption with increasing size despite the lower particle coverage, and while the long wavelength end of the double bump feature at ~375 nm becomes more pronounced, no significant redshift occurs. An absorption feature at 600 to 700 nm appears, which is characteristic of LSPR coupling for dimers and higher-order aggregates (Park et al. 1999; Goulet et al. 2005), and redshifts with increasing particle size.

These results have several implications for the design of NP monolayer-based optical plasmonic devices. Firstly, the increase in absorption and scattering cross section due to increasing particle size trumps the decrease in surface number density, as evident by the taller peak for the NP_5 substrate vs. the NP_1 substrate. However, the solution spectra show opposite behavior, where the Beer-Lambert law holds for increasing concentration. Optical applications which rely on the absorptive strength of monolayers, such as light-trapping layers in thin-film solar cells, may increase absorption by increasing particle size rather than surface density. Also, within this size range, the primary peak at ~375 nm does not shift significantly with particle size, but the plasmon-coupled feature at ~600 nm does. The EF in SERS is largest when the LSPR maximum corresponds to the molecular resonance condition (Haynes and Van 2003), so SERS-based sensors may be optimized for specific analytes by tuning particle size for a specific resonance condition. It will be seen in the next section that the drop in particle surface density does not cause significant signal loss.

Particle size effect on SERS

Raman spectra of the substrates were taken by dropping 3 μL of analyte on the substrate and flattening the droplet with a 5 mm × 5 mm glass coverslip. The substrates were used within 3 h of fabrication and drying. R6G at a concentration of 10^{-5} M (4.4 ppm) was used for SERS measurements. Concentrations of less than 10^{-6} M were not stable and results fluctuated. Figure 5 shows the Raman spectrum of the NP_1 substrate with pure water

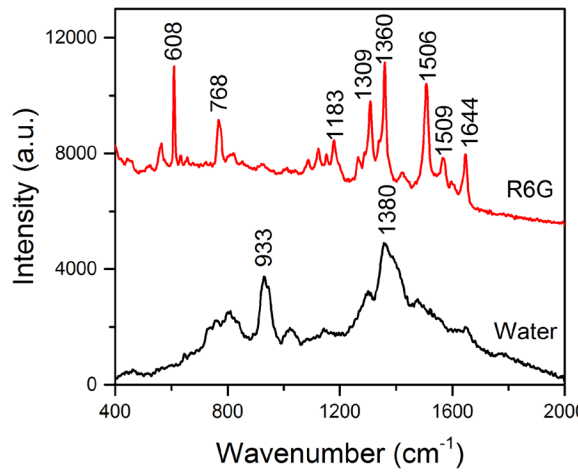

Fig. 5 Raman spectrum of *(bottom)* bare NP_1 substrate and *(top)* SERS of a droplet of R6G 10^{-5} M on the NP_1 substrate smeared by a glass cover slip. Curves shown are the average of three acquisitions in different spots across the substrate. Because of the statistical uniformity of the NP monolayer within the beam spot (~30 μm), the spot-to-spot signal variation was less than 15%. Spectra were acquired with 4.5 mW laser power at 663 nm excitation with 10 s acquisition time

(bottom) and R6G (top). Two broad peaks occur on the bare substrate, 933 and 1380 cm^{-1}, attributed to the surfactants PVP and TSC left in SERS hotspots from the aggregation stage of monolayer growth. Upon addition of the aqueous R6G, a suppression of the elevated spectral region around the two background peaks is observed, and the characteristic R6G peaks appear. The peak at 608 cm^{-1} corresponds to C-C-C in-plane bending modes, the peaks at 768 and 1183 cm^{-1} are C–H out-of-plane dihedral modes, and the rest of the labeled peaks at a higher wavenumber are associated with C–C aromatic stretch modes (Hildebrandt and Stockburger 1984; Pristinski et al. 2006).

To evaluate the effect of particle size on SERS signal, the peaks at 608, 1183, and 1647 cm^{-1} are chosen for analysis because they are in a relatively flat region of the spectral background. Figure 6 plots the heights of these peaks against the average NP diameter. By using a concentration several orders of magnitude above the single molecule regime, surface adsorption of R6G on silver reaches saturation. This is evident by the lack of

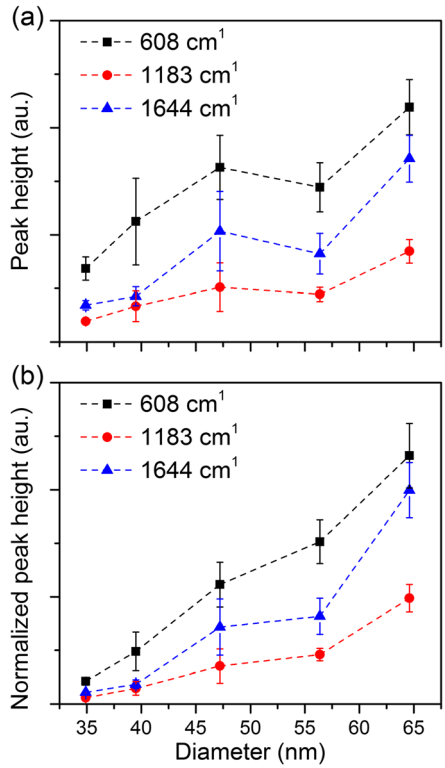

Fig. 6 Dependence of the intensity of selected Raman peaks on the particle diameter **a** without any manipulation and **b** normalized for NP surface density. Peak heights are based on the average of three acquisitions at different positions on the substrate, with error bars indicating standard deviation

notable signal increase at a concentration of 10^{-4} M. To elucidate the effect of particle size, peak heights were then normalized with surface density. A clear increasing trend is seen, consistent with the increasing strength of the substrate LSPR. Interestingly, the increase in signal strength was evident prior to normalization for NP surface density. Due to the highly localized nature and extremely large signal enhancement of SERS hot spots, it is believed a small fraction of analyte molecules adsorbed into hot spots is responsible for the majority of the total SERS signal (Etchegoin et al. 2006). Nonetheless, a signal still increases with size despite the drop in the surface number density. This may be attributed to larger particle size distributions, which may produce various hot spot configurations (Moskovits and Jeong 2004).

In order to verify our results, finite element modeling using COMSOL MultiPhysics (Version 5.0) was used to compute the size dependence of the LSPR in a single particle, and dimer configuration. An incident Gaussian beam excitation is plugged into Maxwell's equations, and the scattered field is solved for. To visualize the LSPR, the electric field norm is computed according to the equation

$$|E| = \left(\vec{\mathbf{E}} \cdot \vec{\mathbf{E}}\right)^{1/2}$$

Figure 7 plots a planar cross section of the electric field norm in the case of 633 nm excitation and 50 nm diameter particles. When in a dimer, a hot-spot forms in the space between particles, and the electric field norm is 15 times stronger than the incident power. Without the dimer, the strongest site on the particle surface is only 3.5 times stronger. While this still represents an enhancement, the SERS EF can be approximated by $|E/E_0|^4$, since intensity is proportional to E^2 and the enhancement occurs twice: on incidence and upon scattering (Le Ru et al. 2006). This fourth power is the source of the dramatic scaling of EF with electric field strength observed in SERS.

A parametric sweep of particle size, gap width, and wavelength was performed, and the resulting EFs are calculated according to $|E/E_0|^4$ and plotted in Fig. 8a. Electric field norms were taken at the center of the gap along the dimer axis. For comparison, the maximum EF on the surface of an individual nanoparticle is shown in Fig. 8b. EFs for dimers are dramatically greater than

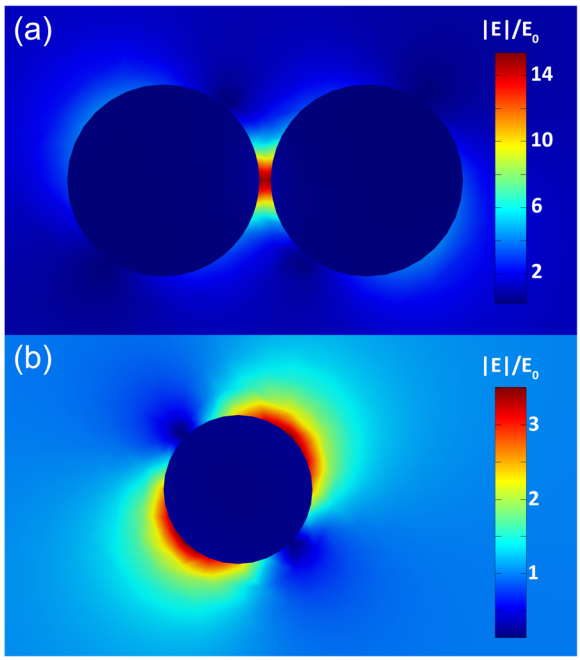

Fig. 7 Visualization of the LSPR for a 50-nm silver nanoparticle dimer with a 2-nm gap and (b) an isolated 50 nm particle. The electric field norm is plotted on the $z = 0$ plane, giving a cross section through the middle of the particles. Incident excitation is a Gaussian beam of wavelength 633 nm, beam waist diameter 3 μms, and $E_0 = 1$ V/m

individual particles, reaching values several orders of magnitude greater. Generally, EFs increase to a peak as particle size increases, and then drop by an order of magnitude. EFs are greater overall with a smaller gap, and peak earlier with shorter wavelength excitation, as expected. A secondary peak occurs due to the emergence of quadrupole resonance modes in larger particles (Kelly et al. 2003). Within the range of particle sizes used experimentally in this study, with a 633 nm excitation, in all cases, the EF monotonically increases. Additionally, the computed EFs are on the order of 10^5 to 10^8. Thus, the simulation-derived EFs are in good agreement with the experimentally observed results, which is also observed in gold NPs (Tian et al. 2013).

Conclusions

Silver nanoparticles from 35 to 65 nm were synthesized, and monolayer substrates of these nanoparticles were fabricated using self-assembly on APTES-functionalized glass slides. The effect of particle size on the substrate, optical properties were studied using UV/vis spectroscopy and SEM imaging, and the SERS performance was studied using R6G as a target analyte. The results indicate that the surface number density of particles decreases as particle sizes increase. Increasing particle size from 35 to 65 nm produces stronger LSPR for an

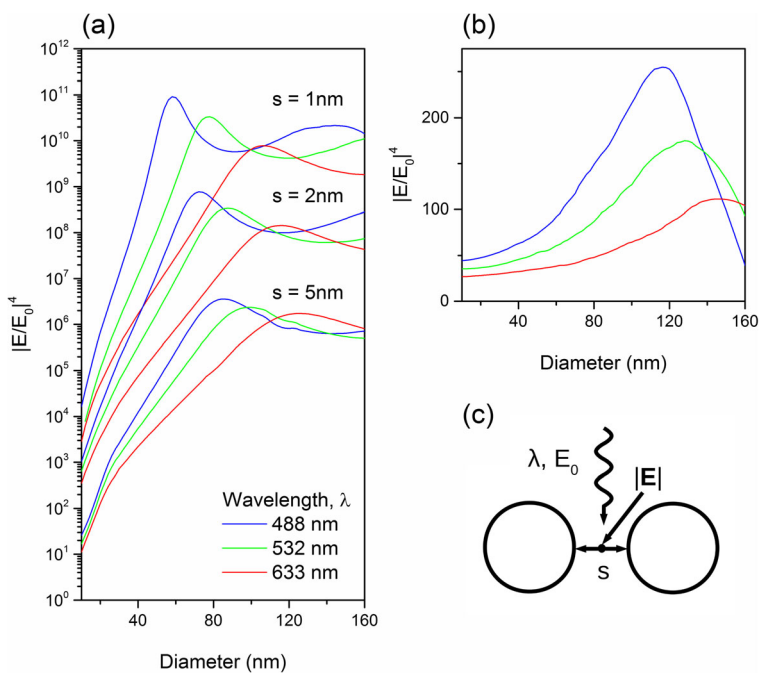

Fig. 8 Plots of simulated enhancement factor (EF) vs. particle diameter **a** for a dimer configuration with various gaps and **b** for a single particle. **c** Schematic depiction of the dimer setup showing where $|E|$ is sampled

excitation of 633 nm and produces larger SERS signals due to optical absorption and scattering of the substrates. This is corroborated by simulation results, which indicate that SERS EF monotonically increases when the separation distance between particles in a dimer decreases and when the particle size increases.

Compliance with ethical standards

Funding This work has been funded by the National Sciences and Engineering Research Council of Canada through a strategic project grant (grant number: STPGP-494554-2016) and the Schwartz-Reisman Foundation through the Waterloo Institute of Nanotechnology–Technion University grant.

Conflict of interest The authors declare that they have no conflict of interest.

References

Alarifi H, Hu A, Yavuz M, Zhou YN (2011) Silver nanoparticle paste for low-temperature bonding of copper. J Electron Mater 40:1394–1402. doi:10.1007/s11664-011-1594-0

Aroca R (2006) Surface enhanced vibrational spectroscopy. Wiley, Chichester

Aslan K, Leonenko Z, Lakowicz JR, Geddes CD (2005) Annealed Silver-Island films for applications in metal-enhanced fluorescence: interpretation in terms of radiating Plasmons. J Fluoresc 15:643–654. doi:10.1007/s10895-005-2970-z

Bastús NG, Merkoçi F, Piella J, Puntes V (2014) Synthesis of highly monodisperse citrate-stabilized silver nanoparticles of up to 200 nm: kinetic control and catalytic properties. Chem Mater 26:2836–2846. doi:10.1021/cm500316k

Behnajady MA, Vahid B, Modirshahla N, Shokri M (2009) Evaluation of electrical energy per order (E EO) with kinetic modeling on the removal of malachite green by US/UV/H 2 O 2 process. Des 249:99–103. doi:10.1016/j.desal.2008.07.025

Bright RM, Musick MD, Natan MJ (1998) Preparation and characterization of ag colloid monolayers. Langmuir 14:5695–5701. doi:10.1021/LA980138J

Chimentão RJ, Kirm I, Medina F et al (2004) Different morphologies of silver nanoparticles as catalysts for the selective oxidation of styrene in the gas phase. Chem Commun:846–847. doi:10.1039/B400762J

Cobley CM, Skrabalak SE, Campbell DJ, Xia Y (2009) Shape-controlled synthesis of silver nanoparticles for plasmonic and sensing applications. Plasmonics 4:171–179. doi:10.1007/s11468-009-9088-0

Dong X-Y, Gao Z-W, Yang K-F et al (2015) Nanosilver as a new generation of silver catalysts in organic transformations for efficient synthesis of fine chemicals. Catal Sci Technol 5:2554–2574. doi:10.1039/C5CY00285K

El Badawy AM, Luxton TP, Silva RG et al (2010) Impact of environmental conditions (pH, ionic strength, and electrolyte type) on the surface charge and aggregation of silver nanoparticles suspensions. Environ Sci Technol 44:1260–1266. doi:10.1021/es902240k

Etchegoin PG, Le Ru EC, Meyer M (2006) An analytic model for the optical properties of gold. J Chem Phys 125:164705. doi:10.1063/1.2360270

Fan M, Brolo AG (2009) Silver nanoparticles self assembly as SERS substrates with near single molecule detection limit. Phys Chem Chem Phys 11:7381–7389. doi:10.1039/b904744a

Goulet PJ, dos Santos DS, Alvarez-Puebla RA et al (2005) Surface-enhanced Raman scattering on dendrimer/metallic nanoparticle layer-by-layer film substrates. Langmuir. doi:10.1021/LA050202E

Grabar KC, Smith PC, Musick MD et al (1996) Kinetic control of interparticle spacing in au colloid-based surfaces: rational nanometer-scale architecture. J Am Chem Soc 118:1148–1153. doi:10.1021/ja952233+

Haiss W, Thanh NTK, Aveyard J, Fernig DG (2007) Determination of size and concentration of gold nanoparticles from UV−Vis spectra. Anal Chem 79:4215–4221. doi:10.1021/AC0702084

Han Y, Lupitskyy R, Chou T-M et al (2011) Effect of oxidation on surface-enhanced Raman scattering activity of silver nanoparticles: a quantitative correlation. Anal Chem 83:5873–5880. doi:10.1021/ac2005839

Haynes CL, Van DRP (2003) Plasmon-sampled surface-enhanced Raman excitation spectroscopy. J Phys Chem B 107:7426–7433. doi:10.1021/JP027749B

Hildebrandt P, Stockburger M (1984) Surface-enhanced resonance Raman spectroscopy of rhodamine 6G adsorbed on colloidal silver. J Phys Chem 88:5935–5944. doi:10.1021/j150668a038

Huynh KA, Chen KL (2011) Aggregation kinetics of citrate and Polyvinylpyrrolidone coated silver nanoparticles in monovalent and divalent electrolyte solutions. Environ Sci Technol 45:5564–5571. doi:10.1021/es200157h

Kelly KL, Coronado E, Zhao LL, Schatz GC (2003) The optical properties of metal nanoparticles: the influence of size, shape, and dielectric environment. J Phys Chem B 107:668–677. doi:10.1021/JP026731Y

Le Ru EC, Etchegoin PG, Meyer M (2006) Enhancement factor distribution around a single surface-enhanced Raman scattering hot spot and its relation to single molecule detection. J Chem Phys 125:204701. doi:10.1063/1.2390694

Le Ru EC, Etchegoin PG, Pablo G (2009) Principles of surface-enhanced Raman spectroscopy: and related plasmonic effects. Elsevier, Amsterdam

Lin T-W, Wu H-Y, Tasi T-T et al (2015) Surface-enhanced Raman spectroscopy for DNA detection by the self-assembly of ag nanoparticles onto ag nanoparticle–graphene oxide nanocomposites. Phys Chem Chem Phys 17:18443–18448. doi:10.1039/C5CP02805A

Morga M, Adamczyk Z, Oćwieja M, Bielańska E (2014) Hematite/silver nanoparticle bilayers on mica – AFM, SEM and streaming potential studies. J Colloid Interface Sci 424:75–83. doi:10.1016/j.jcis.2014.03.005

Moskovits M, Jeong DH (2004) Engineering nanostructures for giant optical fields. Chem Phys Lett 397:91-95. doi: 10.1016/j.cplett.2004.07.112

Oćwieja M, Adamczyk Z, Kubiak K (2012) Tuning properties of silver particle monolayers via controlled adsorption–desorption processes. J Colloid Interface Sci 376:1–11. doi:10.1016/j.jcis.2012.02.017

Oćwieja M, Morga M, Adamczyk Z (2013) Self-assembled silver nanoparticles monolayers on mica-AFM, SEM, and electrokinetic characteristics. J Nanopart Res 15:1460. doi:10.1007/s11051-013-1460-5

Oćwieja M, Adamczyk Z, Morga M, Kubiak K (2015) Silver particle monolayers — formation, stability, applications. Adv Colloid Interf Sci 222:530–563. doi:10.1016/j.cis.2014.07.001

Park S-H, Im J-H, Im J-W et al (1999) Adsorption kinetics of Au and Ag nanoparticles on functionalized glass surfaces. Microchem J 63:71–91. doi:10.1006/mchj.1999.1769

Pristinski D, Tan S, Erol M et al (2006) In situ SERS study of rhodamine 6G adsorbed on individually immobilized ag nanoparticles. J Raman Spectrosc 37:762–770. doi:10.1002/jrs.1496

Qin Y, Ji X, Jing J et al (2010) Size control over spherical silver nanoparticles by ascorbic acid reduction. Colloids Surfaces A Physicochem Eng Asp 372:172–176. doi:10.1016/j.colsurfa.2010.10.013

Rao VK, Abhinav V, Karthik PS, Singh SP (2015) Conductive silver inks and their applications in printed and flexible electronics. RSC Adv 5:77760–77790. doi:10.1039/C5RA12013F

Ricco J-B (2006) InterGard silver bifurcated graft: features and results of a multicenter clinical study. J Vasc Surg 44:339–346. doi:10.1016/j.jvs.2006.03.046

Schrand AM, Braydich-Stolle LK, Schlager JJ et al (2008) Can silver nanoparticles be useful as potential biological labels? Nanotechnology 19:235104. doi:10.1088/0957-4484/19/23/235104

Shahid-ul-Islam S-I, Butola BS, Mohammad F (2016) Silver nanomaterials as future colorants and potential antimicrobial agents for natural and synthetic textile materials. RSC Adv 6:44232–44247. doi:10.1039/C6RA05799C

Stiles PL, Dieringer JA, Shah NC, Van Duyne RP (2008) Surface-enhanced Raman spectroscopy. Annu Rev Anal Chem 1:601–626. doi:10.1146/annurev.anchem.1.031207.112814

Tan H, Santbergen R, Smets AHM, Zeman M (2012) Plasmonic light trapping in thin-film silicon solar cells with improved self-assembled silver nanoparticles. Nano Lett 12:4070–4076. doi:10.1021/nl301521z

Tejamaya M, Römer I, Merrifield RC, Lead JR (2012) Stability of citrate, PVP, and PEG coated silver nanoparticles in ecotoxicology media. Environ Sci Technol 46:7011–7017. doi:10.1021/es2038596

Tian X-D, Liu B-J, Li J-F et al (2013) SHINERS and plasmonic properties of au Core SiO_2 shell nanoparticles with optimal core size and shell thickness. J Raman Spectrosc 44:994–998. doi:10.1002/jrs.4317

Wang M, Sun C, Wang L et al (2003) Electrochemical detection of DNA immobilized on gold colloid particles modified self-assembled monolayer electrode with silver nanoparticle label. J Pharm Biomed Anal 33:1117–1125. doi:10.1016/S0731-7085(03)00411-4

Wang L, Sun Y, Li Z (2015) Dependence of Raman intensity on the surface coverage of silver nanocubes in SERS active monolayers. Appl Surf Sci 325:242–250. doi:10.1016/j.apsusc.2014.11.071

Yu J, Dai G, Huang B (2009) Fabrication and characterization of visible-light-driven Plasmonic Photocatalyst ag/AgCl/TiO_2 nanotube arrays. J Phys Chem C 113:16394–16401. doi:10.1021/jp905247j

Zhao L, Kelly KL, Schatz GC (2003) The extinction spectra of silver nanoparticle arrays: influence of Array structure on Plasmon resonance wavelength and width†. J Phys Chem B 107:7343–7350. doi:10.1021/JP034235J

Zhu S, Fan C, Wang J et al (2013) Self-assembled ag nanoparticles for surface enhanced Raman scattering. Opt Rev 20:361–366. doi:10.1007/s10043-013-0065-7